Journal of Civil, Construction and Environmental Engineering
2025, Vol. 10, No. 6, pp. 262–273
https://doi.org/10.11648/j.jccee.20251006.16

Research Article

The Seismic Performance of RC Frame Structures with Exterior-Hanging Green Self-Insulating Wall

Tingting Li, Xiaowei Li[*], Jiaxin Liu

School of Civil Engineering and Architecture, Southwest University of Science and Technology, Mianyang, China

Abstract

Currently, concrete wall panels have gained widespread attention from the global academic community, but there is relatively little research on concrete sandwich exterior-hanging walls. Based on relevant research by domestic and international scholars on multilayer walls, a novel exterior-hanging green self-insulating wall (EHGSW) has been proposed. Three full-scale frame specimens were constructed: one pure frame, one exterior-hanging wall frame without windows, and one exterior-hanging wall frame with windows. A sliding connection joint was placed between the upper end of the walls, while two load-bearing connection joints were placed at the lower end of the walls. The slotted hole of the sliding connections joint was limited to be 25 mm. Through low cyclic loading tests, the failure modes and seismic performance of reinforced concrete (RC) frame structure with the EHGSW were studied, focusing on seismic behaviors such as hysteresis curves, envelope curves, ductility, stiffness degradation, and energy dissipation capacity. The results indicated that the specimens exhibited flexural-shear failure at the low-ends of the RC columns and the both ends of the RC beams, leading to the development of plastic hinges. When the relative drift between the wall panel and the frame reached the limit of the slotted hole, the stiffness increased sharply. After the failure of the upper sliding connection joint, the hysteresis curves of specimens K2 and K3 were remained consistent with those of specimen K1. The strength degradation factor of the specimens ranged from 0.88 to 0.94. The ductility index of specimens K2 and K3 were between 4.51 and 6.78, it has been improved compared with the pure frame specimen K1 (ductility index of 2.89). The energy dissipation factor of the specimens varied within the range from 0.07 to 0.181.

Keywords

Frame Structure, Seismic Performance, Exterior-Hanging Wall, Self-Insulation, Connection Joints

1. Introduction

With the rapid development of prefabricated buildings in recent years, prefabricated concrete external wall (PCEW), as a kind of enclosure structure, have been widely used in prefabricated buildings. PCEW have developed rapidly due to their advantages such as convenience, durability, thermal insulation and environmental friendliness, have been studied by many scholars. In countries such as Europe and Japan, the research on PCEW has formed a system and a series of applications have been carried out.

With the continuous increase in building energy consumption and environmental pressures, the problems of resource consumption and ecological damage caused by traditional concrete aggregate mining have become increasingly prominent [1]. In recent years, experts and scholars at home and

[*]Corresponding author: lilixxxwww@126.com(Xiaowei Li)

Received: 10 September 2025; **Accepted:** 3 November 2025; **Published:** 11 December 2025

abroad have been committed to developing green wall materials that combine thermal insulation and mechanical properties, promoting their development towards diversification and multi-function. For example, Ma et al. proposed a composite wallboard made of ceramsite concrete, which inputs the insulation materials in between two wallboards to not only solve the fire prevention problem of the insulation materials thoroughly, but also prevent peeling-off of insulation wall during the construction and using processes [2]. Lu et al. proposed that concrete specimens exhibit good performance when the substitution rate of solid-waste-incineration-ash for natural river sand ranges from 0% to 41.3% [3]. Ali et al. presented an innovative approach by integrating textile waste into lightweight precast concrete walls. Results demonstrated that the textile-infused concrete walls exhibit strong seismic performance [4].

To investigate the seismic performance of exterior-hanging walls, in recent years, many researchers have focused on the seismic behavior of autoclaved lightweight concrete (ALC) panel in frame structures. Wang et al. studied the seismic behavior and failure modes of square concrete-filled steel (CFST) tube frames with ALC panels. Results showed the embedded ALC panels greatly improve the stiffness and strength of square CFST frame compared with the external ALC panels [5]. Li et al. explored the seismic performance of H-shaped steel frames with infill precast ALC panels. The failure mode, bearing capacity, stiffness and strength degradation, as well as energy dissipation performance were compared and discussed. The results showed that the infill ALC panels greatly enhance the seismic performance of the frames and has a significant influence on the bearing capacity, stiffness, energy dissipation capacity, and ductility performance of the specimens [6].

To study the connection methods between wall panels and frames, Vaghei et al. used two U-shaped steel channels to connected adjacent prefabricated wall panels. The study showed that the prefabricated connectors can absorb the energy of the prefabricated walls under dynamic loading, thereby improving their seismic performance [7]. Zhao et al. proposed the use of sliding anchor plates and sliding joints to reduce the interaction between the frame and the panels through a sliding mechanism [8]. Biondini et al. developed a model for a frame structure with exterior wall panels, each of which was connected to the frame by two joints at the top and bottom. By gradually increasing the stiffness of the top and bottom joints, the exterior wall panels gradually became part of the lateral resistance system of the primary structure [9]. Ding et al. carried out a cyclic test of a steel frame with ALC panels, proposed a novel pendulous Z-plate connector, and indicated that the new connector can reduce the damage of ALC panels and maintain the safety of the steel frames [10].

Previous studies have mainly focused on industrial solid waste materials and infill walls composed of materials such as bricks, concrete blocks and ALC panels, with relatively few studies on concrete external hanging walls. To investigate the seismic performance of PCEW, this study used waste concrete and aerated soil to fabricate the inner core and inner and outer concrete layers of exterior walls. Low cyclic loading tests were conducted to study the failure modes of the RC frame with EHGSW. The seismic performance of the EHGSW was analyzed, and the shear deformation formula of EHGSW was established.

2. Experimental Design

A sliding connection joint was installed between the upper part of the exterior wall and the frame, as shown in Figure 1, and the dimensions were shown in Table 1. The external wall was secured to the frame via connecting joints, with two sliding connectors at the upper end and two load-bearing connectors at the low end of the wall. The sliding connectors feature a 25 mm slotted hole travel.

Table 1. *Joint dimensions.*

Location Number	Dimensions (mm)
a	100
b	110
c	250

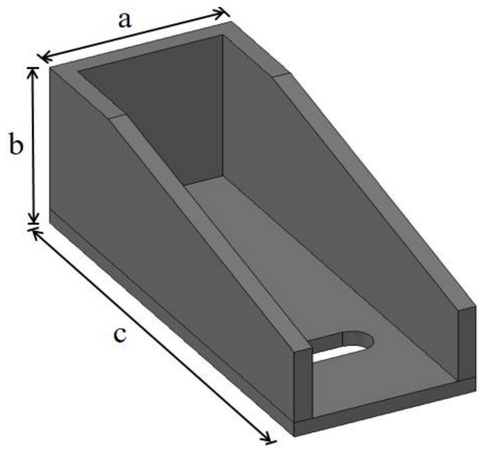

Figure 1. *Sliding connection joint.*

Three specimens were designed, one RC pure frame (denoted by the symbol K1), one exterior-hanging wall frame with windows (denoted by the symbol K2), and one exterior-hanging wall frame without windows (denoted by the symbol K3). the schematic diagrams of the specimens are shown in Figure 2, The details of specimens are listed in Table 2.

Table 2. *Details of Specimen.*

Specimen Number	**K1**	**K2**	**K3**
Type	/	With Window	Without Window
Dimensions (mm)	/	3300×3300×200	3300×3300×200
Column Section(mm)	350×350	350×350	350×350
Beam Section(mm)	350×250	350×250	350×250

(a) (b) (c)

Figure 2. *Schematic diagram. (a) K1, (b) K2, (c) K3.*

The reinforcement of the column and the beam is shown in Figure 3. The reinforcement is represented according to the method described in reference [11]. The frame of specimens K1, K2 and K3 has the same reinforcement.

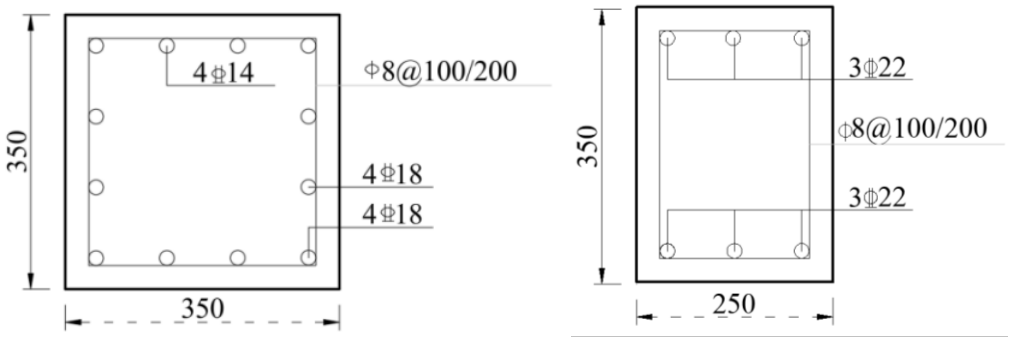

(a) (b)

Figure 3. *Reinforcement details. (a) Column section, (b) Beam section.*

A 100 mm wide concrete rib was set around the wall panel and the opening, as well as at the location of the embedded steel plates, to enhance the integrity and lateral bending resistance of the EHGSW. For specimen K2, a grade of HRB400-grade steel rebars with a 14 mm diameter were selected as the reinforcement around the opening section.

The production and placement of the cement-based porous thermal insulation soil core material for the wall panels are shown in Figure 4.

(a) (b)

Figure 4. *The cement-based porous thermal insulation soil core (a) Production, (b) Installation.*

To ensure the installation accuracy of the wall, first connect the upper sliding connection joint to the embedded part of the top beam through bolts, and then weld it to the embedded steel plate at the top of the wall panel. Finally, weld the lower load-bearing connection joints to the embedded steel plates at the bottom of the wall panels and the bottom beams.

The frame of the specimen was made of C25 commercial concrete. The inner and outer panels of the EHGSW were made of C40 recycled concrete. C40 recycled concrete used solid waste and other resources to replace part of the natural resources. The mix proportion is shown in Table 3.

Table 3. *Mix proportions of concrete (kg•m^{-3}).*

Batch	**5.16**	**5.30**
Cement	290	290
Fly Ash	290	290
Water Reducer	2400	1160
Water	139	197
Recycled Sand from Construction Waste	764	955
Recycled Aggregate from Construction Waste	826	826
Sodium Gluconate Retarder	0.0226	0

3. Material Properties

The inner core material of the EHGSW is made from aerated soil, using waste soil combined with a physical foaming process to prepare a cement-based composite porous material. The mix ratios of cement-based porous insulation soil core materials is shown in Table 4.

In accordance with the Standard for Test Methods of Concrete Physical and Mechanical Properties [12], mechanical property tests were conducted on the insulation soil core materials of each batch of concrete and aerated soil, with specimen sizes of 150 mm×150 mm ×150 mm. The resulting cubic compressive strength is shown in Table 5.

The tested reinforcing bars included three steel grades: HRB400, HPB300, and CRB550. The mechanical parameters of these bars measured in accordance with the " Tensile testing of metallic materials " standard [13] are shown in Table 6.

Table 4. The mix ratios of soil cement-based porous insulation soil core material. (kg·m⁻³).

Ingredient	Weight
Cement	180
Soil	540
Water	290
Cellulose Ether	0.18
Aluminum Sulfate	3.6
Polypropylene (PP) Fiber	0.36
Sodium Sulfate	3.6
Foam	56

Table 5. Concrete of beam and column.

Group	f_{cu} (MPa)
Frames K1, K2, and K3	25.3
Concrete Layer of Wall Panel	41.8
Soil Core Material	0.19

Table 6. Mechanical parameters of steel bars

Grade	Diameter (mm)	Yield Strength *fy* (MPa)	Ultimate Strength *fu* (MPa)
HRB400	12	425	565
	14	440	575
	18	445	600
	22	420	580
HPB300	8	415	580
CRB550	5.3	601	805

4. Experimental Program

4.1. Setup

The specimen was fixed to the ground beam using ground anchor bolts. Lateral braces were placed at both sides of the top beam, and lateral constraints were applied using pulleys to prevent out-of-plane instability during the experiment. Testing setup is shown in Figure 5.

4.2. Instruments

The configuration of the instruments was shown in Figure 5. The linear transformers (L-1 and L-2) were arranged at the diagonals of the frame to measure the shear deformation in specimens. Four displacement gauges, namely F1, F2, F3 and F4, were arranged to measured relative drift between wall panels, while F5–F6 were used to detect vertical displacement of the ground beam. F7–F8 were arranged at both ends of the ground beam to monitor the overall drift of the specimens. F9 automatically collected the drift of between the top beam of the frame under the low cyclic loading tests. Strain gauges were respectively pasted on the surfaces of concrete and reinforcing bar at the top and bottom of the columns and at both ends of the beams to measure the strain of the concrete and reinforcing bars.

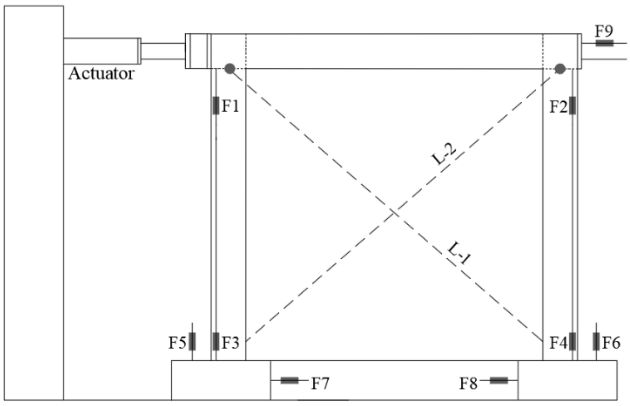

Figure 5. Setup and arrangement.

4.3. Loading Procedure

In accordance with the Building Seismic Testing Code [14], drift-controlled method was adopted. The loading procedure is shown in Figure 6. The specimen was pushed to the right in a positive direction and pulled to the left in a negative direction, which corresponds to the push-pull direction of the actuator. The loading scheme is outlined as follows: First, control drifts of 2 mm, 5 mm, 10 mm, and 15 mm, with each drift applied in one cycle. Next, control drifts of 20 mm, 30 mm, 40 mm, 60 mm, 80 mm, 100 mm, and 120 mm, with each drift applied in three cycles. Finally, control drifts of 140 mm, 160 mm, and 180 mm, each applied in one cycle. Cycling was continued until the lateral load decreased to 85% of the maximum load, at which point the test stopped.

5. Results and Analysis

5.1. Phenomenon

Based on the experimental observations, the overall failure mode of the specimen can be categorized into three stages according to the loading drift: when the loading drift is less than 8 mm, between 8 mm and 40 mm, and greater than 40 mm.

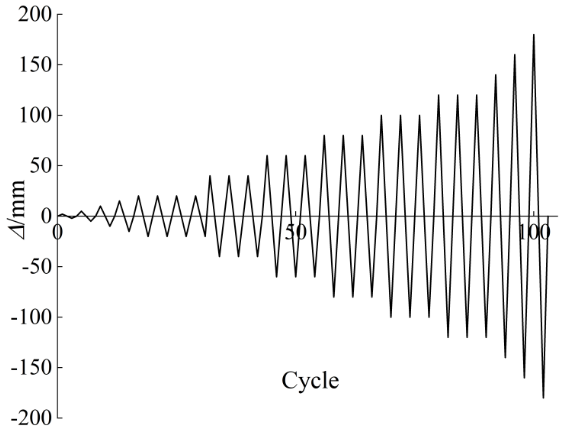

Figure 6. *Loading procedure.*

For the K1 specimen, when the loading drift was less than 8 mm, the specimen borne relatively small loads, with no crack occurred, and the structure was in the elastic stage. When the loading drift was between 8 mm and 40 mm, cracks developed progressively at the low-ends of the RC columns and at the beam-column connection joints. The concrete at the cracked locations no longer borne tensile stress, while the stress in the steel reinforcement increased. As the loading drift increased, the stress in the steel reinforcement reached its yield strength. After the loading drift exceeded 40 mm, cracks developed rapidly, with longitudinal cracks appeared in the compressed concrete area, resulted in a chaotic crack network. As the loading drift completely increased, the concrete is completely crushed, and a plastic hinge forms at the low-ends of the RC columns, with shear failure occurred at the beam-column connection joint, as shown in Figure 7(b).

(a) (b) (c)

Figure 7. *Crack patterns of specimen K1. (a) Low-ends of the left column, (b) Low-ends of the right column, (c) Beam–column joint.*

(a) (b) (c)

Figure 8. *Crack patterns of specimen K2. (a) Connection between bottom beam and load-bearing joint, (b) Sliding connection joint, (c) Top of column.*

The failure mode of the specimen K2 during the experiment was similar to that of the specimen K1. When the loading drift was less than 10 mm, the wall panel underwent relative sliding with the frame through the sliding connection joint, with the load being borne by the frame. As the loading drift ranged from 10 mm to 40 mm, the relative drift between the wall panel and the frame reached the maximum load at the sliding connection joint, and the wall panel and frame shared the load. As the loading drift increased, the embedded anchor bars in the sliding connection joint fractured. When the loading drift exceeded 40 mm, the frame borne the load independently, and the wall panel was connected to the frame through the load-bearing connection joints, while the wall panel maintained good safety and stability.

The test phenomena and failure modes of the K3 specimen were basically the same as those of the K2 specimen. When the load reaches 40mm, the upper connection node fails. With the increased of the loading displacement, the frame structure borne the load, forming a plastic hinge at the top and base of the column.

Specimens K1, K2 and K3 all formed plastic hinges at low-ends ofthe column. Before micro-cracks appear in the beam, there are micro-cracks at the joints, but the presence of stirrups can limit the development of micro-cracks.

5.2. Hysteresis Curves

The hysteresis curves for each specimen group are shown in Figure 9. As shown in the figure, when the drift of the specimen is less than 8 mm, the hysteresis curves exhibited a "spindle" shape, and the specimens are mainly in an elastic working state at this time. As the drift ranges from 8 mm to 80 mm, the hysteresis curves transform into an inverse "S" shape. Energy dissipation is concentrated on crack initiation and propagation. When the drift exceeds 80 mm, cracks at the low-ends of the columns and beam-column joints continue to deepen, and the bearing capacity of the specimens shows a significant decrease.

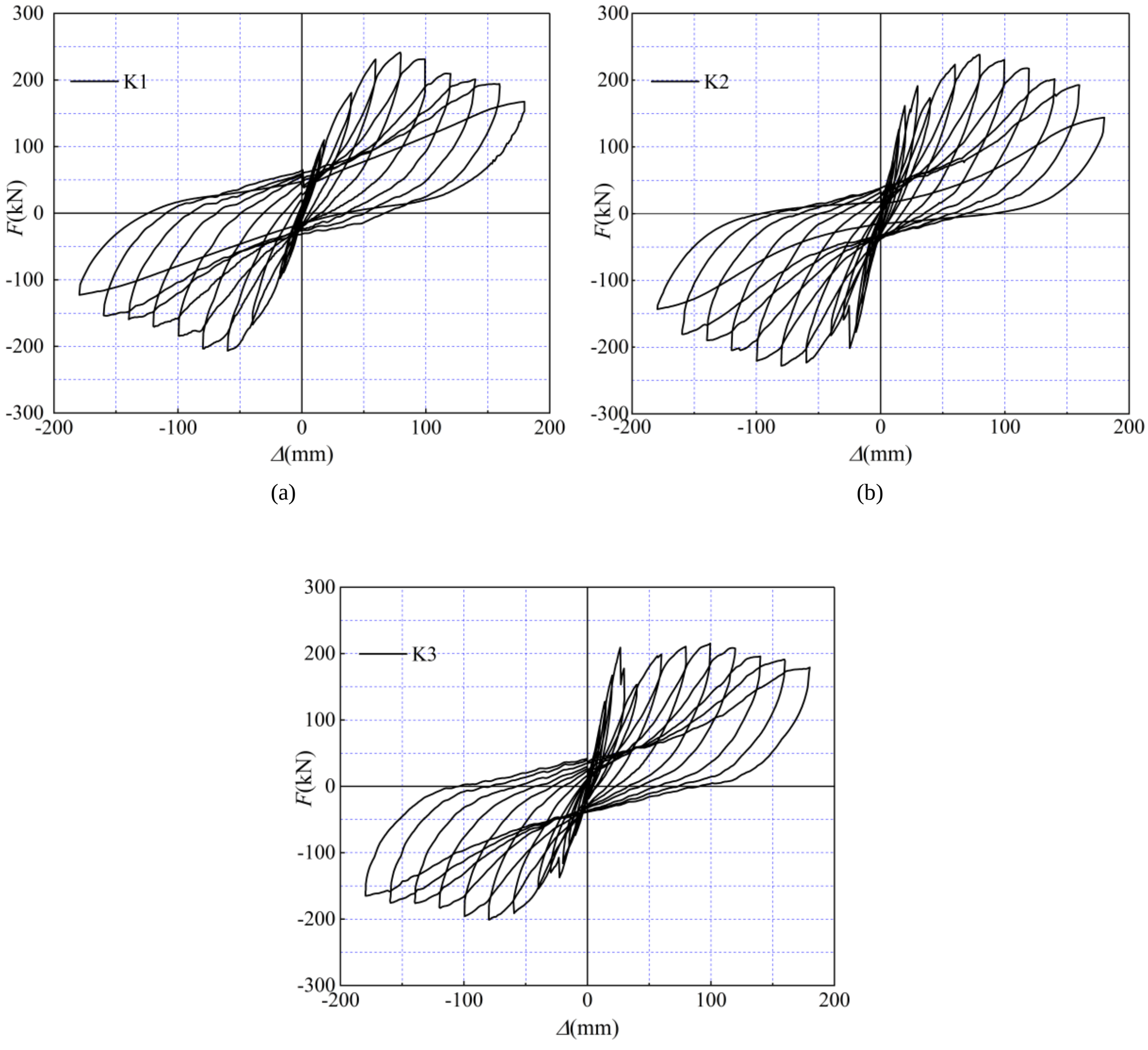

Figure 9. Hysteresis Curves (a) K1, (b) K2, (c) K3.

5.3. Skeleton Curves

The skeleton curves for each specimen group are shown in Figure 10. As can be seen from the figure, the three specimens are in the elastic phase during the initial loading phase, the skeleton curves of each specimen remain basically consistent. With the increase of drift, the K2 and K3 specimens reach the limit of the slotted hole, and the slope of the curve increases significantly. When the drift reaches 25 mm, the horizontal load of K2 and K3 specimens reaches the bearing capacity limit of the sliding connection joints. Compared with specimen K1, under the same drift, the sliding connection joints participating in the structural force improved the load-bearing capacity of the structure. However, after the brittle failure of the joints, the peak loads of the skeleton curves for all three specimens are basically the same.

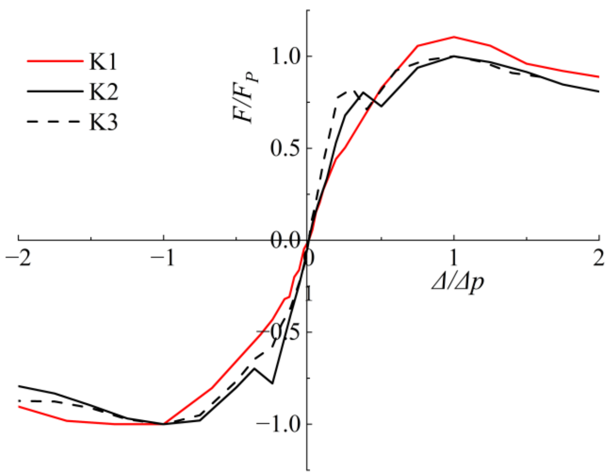

Figure 10. *Skeleton Curves.*

5.4. Ductility Index

The characteristic points of each specimen are shown in Table 7. It can be known from the table that the yield point drift of the specimens is between 25.3 mm and 44.6 mm, and the yield point load is between 147.5kN and 203.1kN. The peak point drift of the specimen ranges from 60.0 mm to 99.5 mm, and the peak point load ranges from 200.9kN to 241.6kN. The drift at the limit point of the specimen is between 112.1mm and 173.5mm, and the load at the limit point is between 170.7kN and 205.3kN.

The magnitude of structural ductility is typically expressed using the ductility index β, which is defined as follows:

$$\beta = \Delta u / \Delta y \tag{1}$$

in which Δu is the ultimate drift, and Δy is the yield drift.

The ductility index of specimens K2 and K3 are between 4.51 and 6.78, which is higher than the pure frame specimen K1 (ductility index of 2.89), indicating that the EHGSW system has good ductility deformation performance.

According to the Chinese standard of the Code for Seismic Design of Buildings (GB50011-2010)[15], for concrete frame structures, the value of 1/550 is the elastic inter-story drift rotation limit, the value of 1/50 is the elastic-plastic inter-story drift rotation limit. As shown in Table 7, the elastic drift ratios of all specimens range from 1/119 to 1/67, significantly exceeding the code-specified limit of 1/550 for RC frame structures under elastic conditions. Meanwhile, the ultimate drift ratios fall between 1/27 and 1/17, exceeding the value 1/50 for elastic-plastic inter-story drift rotation limit of concrete frame structures.

Table 7. *Key Points.*

SN	LD	Yield Point		Peak Point		Ultimate Point		EDR	UDR	DI
		Δ_y/ mm	F_y/kN	Δ_p/ mm	F_P/kN	Δ_u/ mm	F_u/kN			
K1	Positive	44.6	192.9	79.3	241.6	128.9	205.3	1/67	1/23	2.89
	Negative	39.5	166.6	60.0	206.5	112.1	175.5	1/76	1/27	2.84
K2	Positive	30.8	189.4	79.2	238.3	138.9	202.5	1/97	1/22	4.51
	Negative	25.3	201. 1	80.0	227.9	134.4	193.7	1/119	1/22	5.31
K3	Positive	25.6	203. 1	99.5	215.4	173.5	183. 1	1/118	1/17	6.78
	Negative	33.0	147.5	79.4	200.9	168.5	170.7	1/91	1/18	5. 11

SN: Specimen Number, LD: Loading Direction, EDR: Elastic Drift Rotation, UDR: Ultimate Drift Rotation, DI: Ductility Index.

5.5. Strength Degradation

The calculation formula for the strength degradation factor is shown as follows.

$$\lambda_i = F_i / F_{i-1} \quad (2)$$

in which λ_i is the strength degradation factor for the i-th cycle; F_i is the peak load of the i-th cycle; F_{i-1} is the peak load of the previous cycle.

The strength degradation factors of each specimen are shown in Figure 11. As can be seen from the figure, the positive strength degradation factor varies within the range of 0.55 to 1.12. When the ductility ratio (Δ/Δy) is less than 1.2, the negative strength degradation factor is between 0.75 and 1.15. With the continuous increase in ductility ratio, the strength degradation factors of each specimen decreased. Eventually, the strength degradation factors of the three specimens stabilized within the range of 0.88 to 0.94.

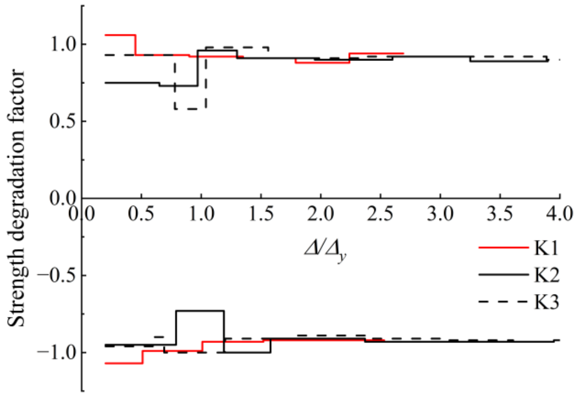

Figure 11. *Strength Degradation Curves.*

5.6. Stiffness Degradation

The calculation formula for the secant stiffness is shown as follows:

$$k_j^i = \sum_{i=1}^{n} F_j^i / \sum_{j}^{n} \Delta_j^i \quad (3)$$

in which k_j^i is the secant stiffness, F_j^i is the lateral load, Δ_j^iji is the drift, 'i' is the number of cycles, and 'j' is the intended drift.

The stiffness degradation curves for each specimen group are shown in Figure 12. From the graph, it can be observed that and that the effective stiffness decreases as the ductility ratio increases. When the ductility ratio of the K1 specimen is less than 1, the stiffness curve decreases rapidly. At this time, the specimen mainly shows that new cracks constantly occur in the RC columns and the RC beams, and the original cracks continue to develop and deepen. As the ductility ratio increases, the rate of curve decline of the specimen slows down from the yield point to the ultimate load point, and the decrease in stiffness also slows down accordingly. At this stage, the specimen suffered relatively severe damage, forming plastic hinges at the low-ends of the RC columns and the both ends of the RC beams. When the ductility ratio of K2 and K3 specimens is less than 0.5, the stiffness deteriorates rapidly. As the ductility ratio increases from 0.5 to 1.0, the rate of stiffness degradation gradually slows down after the ductility ratio is greater than 1.0.

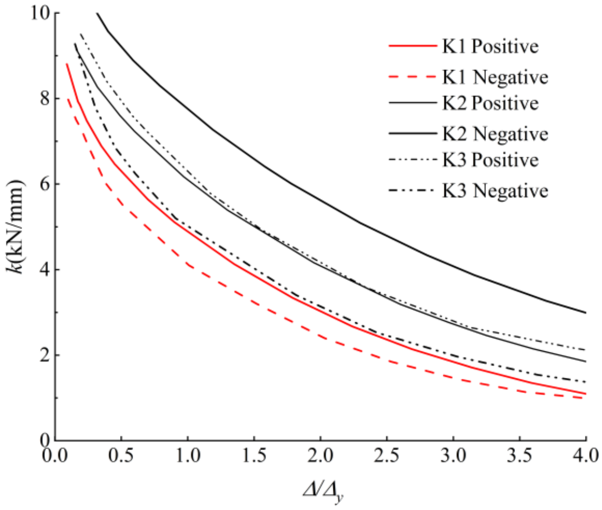

Figure 12. *Stiffness Degradation Curves.*

5.7. Energy Dissipation

The area enclosed by its hysteresis loop（shown in Figure 13)is related to the amount of energy dissipated..

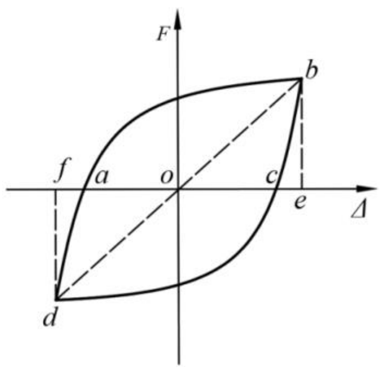

Figure 13. *Diagram for Calculation of Structural Energy Dissipation Coefficient.*

Generally speaking, the equivalent viscous damping factor (*he*), commonly used to measure the energy dissipation capacity of a system. The equivalent viscous damping factor (*he*) can be calculated by the formula:

$$h_e = \frac{1}{2\pi} \cdot \frac{S_{(ABC+CDA)}}{S_{(OBE+ODF)}} \tag{4}$$

in which *he* is the equivalent viscous damping factor, $S_{(ABC+CDA)}$ is the area enclosed by the curves of ab-bc-cd-da. $S_{(OBE+ODF)}$ is the area enclosed by the polyline of o-b-e and o-d-f.

Table 8 and Figure 15 show the energy dissipation factors and equivalent viscous damping coefficients of each group of specimens. As can be seen from the figure, the energy dissipation factor of the specimen ranges from 0.22 to 0.57, and the equivalent viscous damping factor ranges from 0.07 to 0.18. The energy dissipation factor of specimen K1 is greater than that of specimens K2 and K3.

Table 1. *Energy Dissipation Indices.*

Specimen Number	Energy Dissipation Factor	Equivalent Viscous Damping Factor
K1	0.22~0.57	0.07~0.18
K2	0.22~0.46	0.07~0.14
K3	0.22~0.52	0.07~0.16

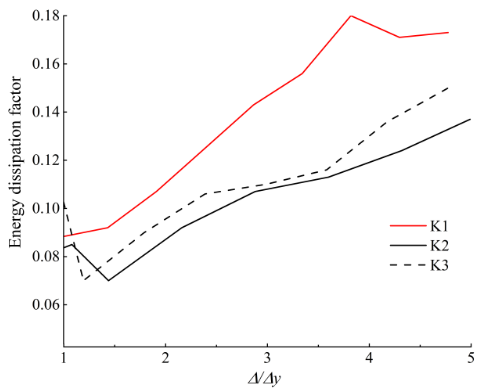

Figure 14. *Curves of Equivalent Viscous Damping Coefficient.*

5.8. Shear Deformation

As shown in Figure 15, the shear deformation *Δs* can be calculated using formula, and the shear angle is determined by formula.

$$\Delta_s = \frac{1}{2}\left(\sqrt{(d_1 + D_1)^2} - (\sqrt{(d_2 + D_2)^2 - h^2})\right) \tag{5}$$

$$\gamma = \Delta_s / h \tag{6}$$

in which *h* is the initial vertical distance between the ends of the wire drift gauges, and *L* is the initial horizontal distance between ends, Δ*s* is the shear deformation, and γ is the shear angle, d_1 and d_2 are the initial distances of the diagonals, while D_1 and D_2 are the measured values of the wire drift gauge respectively.

The correlation between the shear angle (γ) and the loading drift (Δ) is shown in Figure 16. As seen from the figure, the shear angle increases as the loading drift increases.

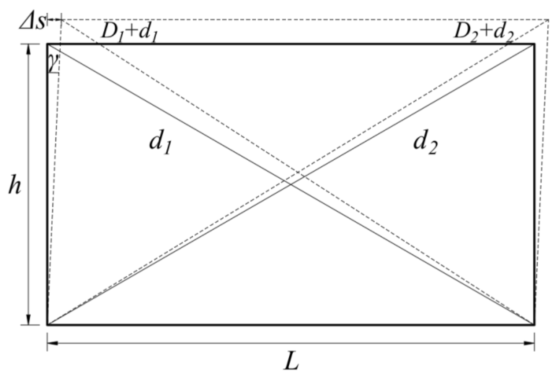

Figure 15. *Shear Deformation.*

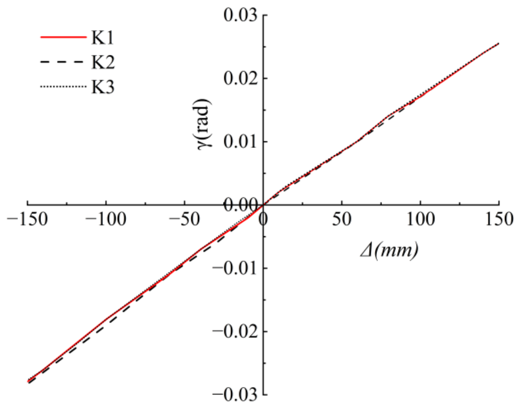

Figure 16. *Shear Angle.*

6. Conclusions

In this study, three specimens were fabricated: one pure frame, one exterior-hanging wall panel frame without windows, and one exterior-hanging wall panel frame with windows.

The seismic performance of the EHGSW was investigated through experimental testing. Based on the test results, the following conclusions could be developed:

1) The specimens experienced flexural-shear failure at the low-ends of the RC columns and the both ends of the RC beams during the test, forming plastic hinges. When the relative drift between the wall panel and the frame reached the limit of the slotted hole, the stiffness increased sharply. After the ductility ratio exceeded 1.0, the stiffness degradation progressively decreased.
2) After the failure of the upper sliding connectors, the hysteresis curves of specimens K2 and K3 were remained consistent with those of specimen K1. The strength degradation factor of the specimens ranged from 0.88 to 0.94. The ductility index of specimens K2 and K3 were between 4.51 and 6.78, it has been improved compared with the pure frame specimen K1 (ductility index of 2.89). The energy dissipation factor of the specimens varied within the range from 0.07 to 0.181.
3) The travel of sliding connectors significantly influences the force transfer between the exterior hanging panels and the frame. To reduce the impact of the exterior hanging panels on the in-plane seismic performance of the frame structure, sliding connectors should be set with an appropriate travel.

   Through the research in this paper, the authors believe that the future research fields of the prefabricated wall panel are as follows: 1) the U-shaped energy dissipation device is set between the frame and the wall panel to increase the energy dissipation capacity and seismic performance of the structure; 2) Adding lightweight ceramsite in the soil core material to further improve the thermal insulation performance of the wall panel and reduce the consumption of cement.

Abbreviations

AAC	Autoclaved Aerated Concrete
RC	Reinforced Concrete
MSWIBA	Municipal Solid Waste Incineration Bottom Ash
ALC	Autoclaved Lightweight Concrete

Acknowledgments

During the course of this research and experimentation, special thanks are extended to the Structural Laboratory of Southwest University of Science and Technology for providing technical support. The authors gratefully acknowledge Professor Xiaowei Li and senior fellow Jiaxin Liu for their valuable suggestions on experimental design and manuscript preparation. Appreciation is also given to colleagues Junchen Xiang, Fenghao Qi, and Haitao Zhao for their assistance during the experiments. Finally, sincere thanks are expressed to all team members and colleagues who contributed to this study.

Author Contributions

Tingting Li: Resources, Software, Investigation, Visualization

Xiaowei Li: Conceptualization, Supervision, Writing–review & editing

Jiaxin Liu: Data curation, Formal Analysis

Funding

This work is supported by the following funds:

1) The Natural Science Foundation of Sichuan Province (Grant No.2022NSFSC0095 & 2022NSFSC0319).
2) The Experimental Technology Research Project of Southwest University of Science and Technology (2024), for the development of "A Multi-Boundary Non-Uniform Constraint Steel-Wood Interface Friction Coefficient Testing Apparatus Based on an MTS Platform".
3) The Natural Science Foundation of Southwest University of Science and Technology (Grant No. 21zx7121), for the research project "Development and Mechanical Performance Study of High-Stiffness and Strong Bend-Resistant Anchored Timber Structural Connections".

Data Availability Statement

The data that support the findings of this study can be found at: https://doi.org/10.1234/jbs.2024.456112

The data is available from the corresponding author upon reasonable request.

The data supporting the outcome of this research work has been reported in this manuscript.

Conflicts of Interest

The authors declare no conflicts of interest.

References

[1] Bio-based aggregate in the production of advanced thermal-insulating concrete with improved acoustic performance. Composites PartB: Engineering. 2022, 248, 110392. https://doi.org/10.1016/j.compositesb.2022.110392

[2] Ma, S., Yu, G., Peng, B., Seismic performance of ceramsite concrete T-shaped composite wallboard joints under cyclic loading. Structures. 2021, 33, 4433–4445. https://doi.org/10.1016/j.istruc.2021.07.023

[3] Lu, J., Yang, X., Lai, Y., Gao, J., Wang, Y., Deng, F., & Zhang, Z. (2024). Mechanical and microscopic properties of concretes made with municipal solid waste incinerator bottom ash (MSWIBA) exposed to freeze-thaw cycles. Construction and Building Materials, 452, 138864. https://doi.org/10.1016/j.conbuildmat.2024.138864

[4] Ali, W., Shahzada, K., Shah, R., Jamshaid, H., & Noor, U. A. (2025). Seismic capacity assessment of lightweight precast concrete infill wall panels with textile waste core in reinforced concrete frame structures. Structures, 79, 109669. https://doi.org/10.1016/j.istruc.2025.109669

[5] Wang, J., Li, B. Cyclic testing of square CFST frames with ALC panel or block walls. Journal of Constructional Steel Research. 2017, 130, 264–279. https://doi.org/10.1016/j.jcsr.2016.12.006

[6] Li, Y., Gao, C., Li, X., Yan, Y., Ning, Z. et al. Experimental study on the seismic performance of steel frames with infill ALC wall panels. Journal of Building Engineering 65, 105739 (2023). https://doi.org/10.1016/j.jobe.2022.105739

[7] Vaghei, R., Hejazi, F., Taheri, H., Jaafar, M. S., & Abdul Aziz, F. N. A. Development of a new connection for precast concrete walls subjected to cyclic loading. Earthquake Engineering and Engineering Vibration. 2017, 16(1), 97–117. https://doi.org/10.1007/s11803-017-0371-3

[8] Zhao, J., Zhang, J., Song, J., Zhou, Y., Bai, J., & Yu, H. Sliding gusset connections for improved seismic performance of BRB-RC frame: Damage-control design and subassemblage tests. Engineering Structures. 2023, 282, 115828. https://doi.org/10.1016/j.engstruct.2023.115828

[9] Biondini, F., Dal Lago, B., & Toniolo, G. Role of wall panel connections on the seismic performance of precast structures. Bulletin of Earthquake Engineering. 2013, 11(4), 1061–1081. https://doi.org/10.1007/s10518-012-9418-z

[10] Ding, K.; Kong, X.; He, S.; Zong, D. Experimental and parametric study on seismic behavior of steel Frame with ALC panels. Buildings 2022, 12, 2070. https://doi.org/10.3390/buildings12122070

[11] 16G101, Plan view overall representation method drawing rules and structural details for concrete structures: Beijing, China, 2016.

[12] GB/T 50081-2019; Standard for Test Methods of Concrete Physical and Mechanical Properties. Standards China: Beijing, China, 2019.

[13] GB/T 228.1-2010; Tensile testing of metallic materials [S]. Beijing: China Standards Press, 2010.

[14] JGJ/T 101-2015, Building Seismic Testing Code, China, 2015.

[15] GB 50011-2010; Code for Seismic Design of Buildings. Standardization Administration of China: Beijing, China, 2010.